Chemotactic interactions drive migration of membraneless active droplets

Mirco Dindo[†1,2], Alessandro Bevilacqua[†1], Giovanni Soligo[3], Alessandro Monti[3], Marco Edoardo Rosti[3], Paola Laurino[1*]

[1]Protein Engineering and Evolution Unit, Okinawa Institute of Science and Technology Graduate University, Onna, 904-0412, Okinawa, Japan.
[2]Department of Medicine and Surgery, Section of Physiology and Biochemistry, University of Perugia, Perugia, 06132, Italy.
[3]Complex Fluids and Flows Unit, Okinawa Institute of Science and Technology Graduate University, Onna, 904-0412, Okinawa, Japan.

*Corresponding author(s). E-mail(s): paola.laurino@oist.jp;

Abstract

In Nature, chemotactic interactions are ubiquitous and play a critical role in driving the collective behaviour of living organisms. Reproducing these interactions *in vitro* is still a paramount challenge due to the complexity of mimicking and controlling cellular features, such as metabolic density, cytosolic macromolecular crowding and cellular migration, on a microorganism size scale. Here we generate enzymatically-active cell-size droplets able to move freely and, by following a chemical gradient, able to interact with the surrounding droplets in a collective manner. The enzyme within the droplets generates a pH gradient that protrudes to the outer edge of the droplets. We discovered that this external pH gradient controls droplets' direction and speed, ultimately inducing migration. Further, we showed that these cellular-like features can facilitate the reconstitution of a simple and linear protometabolic pathway with improved overall activity. Our work suggests that simple and stable membraneless droplets can be applied to reproduce complex biological phenomena *in vitro* opening new perspectives as bioinspired materials and synthetic biology tools.

Keywords: liquid-liquid phase separation, chemotactic interactions, cellular migration, pH gradient

[†]These authors contributed equally to this work

Introduction

Cellular migration represents a key feature of living systems [1–3]. It manifests as the response to a stimulus which drives the directionality of the cellular motility. The migration can be mediated by chemotactic sensing, which plays a critical role in many processes, driving long-range interactions and collective behaviors of living systems, as well as sustaining and regulating life [1]. Chemotactic strategies have been reported to drive cell migration towards a higher chemoattractant molecule concentration, such as glucose, amino acids and other cell nutrients (positive chemotaxis) [4], or towards a lower chemorepellent molecule concentration, such as phenol and other cytotoxic compounds (negative chemotaxis) [5]. Chemotactic interactions also play a significant role in multicellular life, e.g. they are involved in organism development [6], immune response [7], cancer [8, 9] and inflammatory diseases [10]. Due to its fundamental role, current intracellular pathways leading to cellular chemotaxis have been deeply studied [11, 12], but mimicking *in vitro* the cellular degree of complexity is challenging. In fact, how nature has achieved this level of complexity is not completely understood [13, 14]. Studying how these cellular functions work and arise require life-like systems capable of mimicking cellular complex features *in vitro*, such as metabolic density, cytosolic macromolecular crowding, proliferation and migration [15–17]. Thus, reproducing pivotal chemotactic interactions *in vitro* is a key step to unravel basic natural rules driving collective behavior and the physical principles ruling these phenomena.

The design and control of synthetic droplets, protocells or cells able to recall cellular features and respond to chemical signals represent a new frontier for intelligent materials [18, 19] and biotechnology [20–25]. In general, protocells can be obtained by encapsulation in a membrane [26–30] or by liquid-liquid phase separation (LLPS) [31–36]. In the current literature, protocells and artificial droplets systems have been deeply exploited to study cellular features [37–39] or to reproduce them [18, 40–42]. These studies highlight the potential of using protocellular systems to study biologically relevant questions, but also the current limitations and challenges in mimicking the complexity of living systems [28]. In detail, the presence of a not- or semi-permeable membrane strongly affects, or impedes completely, the diffusion of molecules in and out of the protocells, limiting studies on chemotactical sensing [43] or enzyme kinetics [44]. Regarding the membraneless liquid droplets, mainly obtained by LLPS, their behavior is affected by external environmental factors, such as pH, ionic strength or temperature [45] and surrounding molecules. For these reasons, they show poor stability (dissolution, spreading on the surfaces and aggregation) and they do not usually respond to chemical gradients [46]. In conclusion, these studies do not report protocells able to respond to a chemical signal/external stimuli by showing migration triggered by chemotactic sensing.

In this work, we report how enzymatically-active droplets respond and move when triggered by a chemical gradient of pH in a chemotactic manner. The droplet microenvironment not only mimics intracellular features like cytosolic protein crowding, metabolic activity and cell-like length scale, but also resembles intercellular complex interactions such as migration and merging. The enzyme partitioned in the droplets

generates a pH gradient which extends within and outside the droplets, and modifies the surface tension of the droplets according to the local pH. Changes in the surface tension value along the interface of the droplets generate stresses tangential to the interface, known as Marangoni stresses. The Marangoni-induced flow is able to propel the droplet towards the direction that minimizes its surface energy [47], i.e. towards higher values of pH (Fig. 1). A single isolated droplet generates a uniform pH field along the interface; surface tension is thus constant and no Marangoni-induced flow is generated. Conversely, when multiple drops are present, their pH halos superpose and generate inhomogeneity in the pH field along the interface of the droplets, ultimately resulting in Marangoni-induced motion. In summary, droplets influence each other and move towards neighboring ones driven by a difference in pH. Once the protein droplets are close enough to each other, they merge due to their liquid nature and the absence of a membrane. We performed numerical simulations to corroborate the experimental observations, confirming the dynamics of the motion of the droplets. Interestingly, we also demonstrate that our system can trigger and facilitate the formation of a simple linear protometabolic pathway, providing an example and a possible mechanism for long-range interactions in protocell communities.

Results

Generating non-adhering droplets on a glass surface

To avoid glass-adhering phenomena and dissolution of the droplets on the glass slide, several polyethylene glycol diacrylate polymers (PEGDA) were screened as glass slide coatings. The tested polymers were PEGDA 700 Da, PEGDA 4 kDa, PEGDA 6 kDa and PEGDA 10 kDa [48]. In details, we imaged Alexa Fluor 488-labeled BSA droplets using a confocal microscope and we calculated the contact angle formed between the droplet and the coated glass by analyzing 3D images of sessile droplets using the contact angle plug-in of ImageJ software [49]. This analysis measured a contact angle θ (theta) which increases from $114° \pm 5°$ in PEGDA 700 Da to $149° \pm 6°$ using PEGDA 10 kDa (Fig. S1). PEGDA 10 kDa showed the least adhesion of the droplets on the glass slide coating, resulting in spherical droplets that show no resting phenomena on the PEGDA-glass slide surface. For these reasons, PEGDA 10 kDa was chosen as glass slide coating for this study.

Enzymatic activity generates a pH gradient inside and around the droplets

Enzymatically-active urease-containing droplets (1-1.5 μM) (partitioning is reported in Fig. S2) [50] are able to generate a pH gradient inside the droplets and in the nearby external vicinity of the droplet's interface, that we will call herein as the droplets' halo. The basic pH gradient inside and outside the droplets is due to the production of ammonia as a product of urea hydrolysis catalyzed by urease (Fig. S3). We previously studied the droplets inner pH gradient [50]. Here, we study the pH halo features around the droplets and its impact on the droplets and surrounding solution. Using a saturating concentration of urea (115 mM), the intensity of the pH gradient generated

inside the droplets is strictly related to the droplets size, as shown in Fig. 2A and as reported previously [50]. Furthermore, adding 50 μM SNARF in the supernatant phase along with urea 115 mM, we measured the pH of the droplets' halo (Fig. 2B). Our data show that the intensity of the pH gradient around the droplets is strictly related to the intensity of the pH gradient inside the droplets which is closely-related to the droplets size (Fig. 2B). In particular, droplets with radius around 40-50 μm show a higher intensity and amplitude of the pH halo compared to smaller droplets (radius around 8-15 μm) despite containing the same urease concentration (Fig. 2B). This data demonstrated that the halo extension is strictly correlated to the droplet's size.

Migration is driven by a chemical gradient

To understand the effects of droplet migration in solution, we elucidated the parameters that play a role in droplet movements. First, we confirmed that no migration is recorded in the absence of enzymatic activity generated by urease and its substrate, urea. The absence of the substrate urea in the urease-containing droplets (1-1.5 μM), generates no motility (Supporting Movie 1) and no flow inside the droplets [50]. Without urease in the droplets, no migration was detected after adding 115 mM urea in the droplet solution (Supporting Movie 2). Furthermore, if other enzymes that do not produce any detectable pH change were partitioned in the droplets, as lactate dehydrogenase and glucose oxidase (reaction scheme in Fig. S3 and partitioning Fig. S2), no movement of the droplets were observed (Supporting Movie 3 and 4). Importantly, upon addition of a saturating concentration of the substrate urea (115 mM), urease-containing droplets with radius $< 25 - 40$ μm, often showed no migration (Fig. 3A). We hypothesized that a pH gradient of $7-7.5$ is not enough to trigger their movement. To test this hypothesis, another enzyme, cystalysin (reaction scheme Fig. S3 and partitioning Fig. S2), was used to generate a small pH gradient inside the droplets ($\sim$0.5 ΔpH): in this case no movement was recorded, even analyzing big radius droplets ($>$ 70 μm radius) (Fig. S4). These data confirm that the droplets migration in solution is definitely induced by a large pH gradient ΔpH > 0.5 (Fig. 3A). In fact, upon addition of a saturating concentration of the substrate urea (115 mM), droplets with a radius above 40-50 μm generate a ΔpH > 0.5 and show migration towards the surrounding droplets (Fig. 3A).

The droplet migration displayed important features related to droplets size and distance between each other. These mechanisms are described in the three following time sequences: (i) two droplets of approximately the same size (Fig. 3B), (ii) two droplets of different sizes (Fig. 3C) and (iii) several droplets of different sizes (Fig. 3D). The first case reported (Fig. 3B and Supporting Movie 5) shows a merging event of two droplets of 50 μm radius. In this example, the two droplets at an initial distance of 90 μm, are attracted and merge within 120 sec (Fig. 3B). The second case (Fig. 3C and Supporting Movie 6) reports a merging event among droplets of different sizes (of radius equal to $\sim$110 μm and $\sim$60 μm, respectively) at a similar distance of panel B ($\approx$100 μm). It is interesting to note that in this case the droplets still merge, although over a much shorter time (40 sec) compared to the previous case (Fig. 3B, 120 sec). Here the pH halo generated by the larger droplet is wider and higher (according to

Fig. 2), thus speeding up the overall dynamics, as shown in Fig. S8. Lastly, in the multi-droplet case (Fig. 3D and Supporting Movie 7), a droplet of ∼50 um radius displayed an initial migration towards the nearby small droplets (radius of 30-36 μm, snapshots from 0 to 120 sec). Upon merging with these smaller droplets, it changes its migration trajectory being now attracted by the other large droplet (radius of 73 μm, snapshot 120 to 240 sec and Fig. 3E).

All this experimental evidence has been supported by numerical simulations (Fig. 3B-D, and Fig. S5), which consolidate the findings on the direction of the Marangoni-induced motion. Numerical simulations allow us to study the migration of the droplets in simpler configurations, eliminating any long-range effects from far-away droplets, which cannot be singled out in the experiments. The motion of the droplet is induced by the Marangoni stresses acting along the interface: these stresses originate from a non-uniform value of the surface tension along the interface. In particular, Marangoni stresses are directed from low-surface tension regions towards high-surface tension regions and generate a re-circulatory motion inside the droplets [50], which then propels the droplet itself in the direction of its low-surface tension pole, minimizing its total energy [47]. Here the change in surface tension is induced by the local value of pH, as indicated in Fig. S6, where experimental measurements [50] are reported in the inset. Qualitatively, a higher value of pH corresponds to a lower value of surface tension. Marangoni stresses are directed by the surface tension gradient: from low surface tension values (high pH) to high surface tension values (low pH). This results in the droplets moving towards each other, in the direction where the value of the pH is higher (lower surface tension).

In the experiments, the chemical reactions inside the droplet lead to the formation of a pH halo around the droplet itself. For an isolated droplet, the halo is uniform all around the droplet and so is the pH value at the interface. In this case, no Marangoni stresses appear and the droplet is still. This can be appreciated in our numerical simulations, Fig. 3 panels B and C, where upon coalescence of the droplets, the single merged droplet stops moving, as Marangoni stresses are no longer present (surface tension is now homogeneous along the interface). Conversely, in Fig. 3D, upon the first merging, the newly-formed droplet keeps moving: the interaction with the halo generated by the surrounding droplets causes an inhomogeneous pH value (thus, an inhomogeneous surface tension) along the interface, inducing Marangoni stresses along the interface of the droplets, and consequently driving the droplets towards each other.

Another interesting aspect is linked to the strength of the halo: the pH inside the droplet depends on its size, see Fig. 2A. Larger droplets have a higher internal pH value and thus the halo extends further away from the interface of the droplet. When considering smaller droplets, such as those in Fig. S5, we do not observe any motion: the pH inside these (in the range of radius ≈10-40 μm) is rather low (pH≈7 - 7.5), thus the width of the halo is limited. In addition, at these values of pH, the surface tension is roughly constant: small changes in the pH value generate negligible changes in the surface tension value, see Fig. S6. Marangoni stresses in this case are too weak to produce coherent motion of the droplet.

In Fig. 3B-D we report several snapshots from our experiments and numerical simulations representing the three cases previously described: (i) two droplets of

(approximately) the same size (panel B), (ii) two droplets of different sizes (panel C) and (iii) several droplets of different sizes (panel D). In the experiments it is very challenging to obtain binary systems of droplets, in which there is no long-range effect from other droplets further away; numerical simulations allow us to single out these far field effects and focus solely on droplet-droplet interactions. We will thus use data from numerical simulations to show the evolution and interaction of the halos surrounding the droplets, which proved to be fundamental in determining the motion of the droplets.

In Fig. 3B we analyse the case where two droplets of approximately the same size are placed close to each other. Snapshots from the numerical simulations show the evolution of the pH halo around the droplet; the pH halo starts diffusing outwards from the droplets (up to roughly 40 sec, experiment time). Due to the interaction between the halos of the two droplets, the pH is higher in between them, thus generating an imbalance in the pH value along the interface of the droplets. The surface tension gradient due to the pH imbalance generates Marangoni stresses, and ultimately drives the droplets towards each other. The experimental snapshots show that these droplets merge over a ≈ 120 sec time-scale. The lower pH value inside the droplets generates a relatively weaker halo (i.e. extending less off the interface and generating smaller perturbations at the interface of other droplets) compared to larger droplets.

The effect of the droplet size can be understood from the cases shown in Fig. 3C, with two droplets of different sizes placed at a relatively close distance. Similar dynamics are observed for this case as well: the halo diffuses outwards from the droplets in approximately the initial 40 sec (experiment time) and a higher value of pH is found in between the droplets (right pole of the large droplet and left pole of the small droplet). The pH, and thus surface tension, inhomogeneity gereates Marangoni-induced flowing which propels the droplets towards each other. We observe that also the smaller droplet moves: while the internal pH of the droplet is too low to generate motion (i.e. pH≤ 7.5), the pH halo from the larger droplet causes a pH hotspot at the right pole, with local pH values larger than pH$= 7.5$. Upon merging, the droplet in the experiments slowly drifts away, due to the long-range effect of other, out-of-field droplets. In the numerical simulations we do not have effects from other droplets: upon merging there is no longer any imbalance in the halo around the droplet, thus no Marangoni stresses are present. The newly formed droplet does not move any further.

In the third sequence in Fig. 3D we study a multiple-drop case: several droplets of different sizes (and thus different internal pH values) interact with each other. We observe both in our experiments and numerical simulations that larger droplets are those that cover the longest distance and merge into the smaller droplets. The halos generated by the larger droplets extends further away from their interface, and perturbs the pH concentration at the interface of the nearby droplets; closer droplets are clearly subjected to stronger perturbations. The inhomogeneous pH distribution along the interface of the droplets generates a Marangoni-induced flow, which propels the droplets toward each other. When the droplets are close to each other, the pH perturbations at the interface of both large and smaller droplets (here the threshold is about 30-40 μm in radius) is able to generate a non-homogeneous surface tension along the interface, and thus Marangoni-driven self-propulsion. Conversely, when the droplets

are further apart, the halos from other surrounding droplets can modify the surface tension (and thus inducing Marangoni-driven motion) only in the larger droplets, i.e. radius > 30-40 μm. This is also shown in the simulation snapshots: the two smaller droplets on the right are relatively close to each other but will not move until the larger droplet is close enough. This results further corroborates the observation that smaller droplets do not exhibit motility, unless they are in the near proximity of larger ones, as reported in Fig. S5. The larger droplets instead propel themselves according to the surrounding pH gradient, which is given by the superposition of the halos from all the surrounding droplets. These qualitative observations are backed by the trajectories of the center of the droplets, Fig. 3E. Markers on the trajectories are plotted at regular time intervals, thus providing a visual quantification of the speed of the droplets. In both the experiment and numerical simulations, the larger droplets are those covering the longer distances, moving at first towards the closest droplet(s), merging with them and then continuing in their motion for as long as there is an imbalance in the surface tension along their interface. We observe that smaller droplets start moving only when in the near proximity of larger ones, as the latter ones generate a perturbation in the pH field strong enough to significantly modify the surface tension at the interface.

Droplets migration favours the formation of a simple linear protometabolic pathway

Along with the directional movement, these droplets displayed another important feature of liquid-liquid like systems: if two droplets are in proximity, they merge (Fig. 3). In an origin of life scenario, the emergence of metabolic pathways is crucial for the evolution of living systems. From this evolutionary point of view, new metabolic pathways can emerge if different communities (or at least two different protocells/entities) merge and mix their contents in a precise directional way [51, 52]. This scenario would not be favoured if the protocells cannot move or merge. As proof of concept of the importance of migration for reconstituting metabolic pathways, we selected the enzymes pyruvate kinase (PK) and L-lactate dehydrogenase (LDH) (partitioning reported in Fig. S2) to set up a simple two-enzyme pathway inside the droplets. The reaction product of PK is pyruvate (and ATP), which is the substrate of LDH that catalyze, in presence of NADH, the conversion of pyruvate to lactate and NAD^+ (Fig. S3). Confocal microscopy images of droplets containing active unlabeled urease (along with either Alexa Fluor 488 labeled-PK or Alexa Fluor 594 labeled-LDH) show that multienzyme-containing droplets retain their migration feature when triggered by a chemical pH gradient (Fig. 4A and Supporting Movie 8). This leads to the formation of a small and efficient linear pathway by merging two different droplets and mixing efficiently their contents (Fig. 4A). On the contrary, in absence of urease the droplets do not show migration and even when they stochastically merge, they display slower enzymes mixing compared to the active droplets. The slower mixing is due to the absence of Marangoni-induced flow and, thus, based on simple diffusion (Fig. 4B and Supporting Movie 9). To understand how the kinetics of the overall reaction is influenced by the migration, merging and mixing of the droplets, we quantify the production of lactate (the final product of the two-step reaction). In the negative control (Fig. 4C, black squares and line), using separated droplets containing LDH or PK, the

production of lactate is slower compared to droplets containing LDH, PK and urease (Fig. 4C, purple squares and line). This result is in line with the fact that the pyruvate produced by the droplets with PK needs to diffuse out from the droplets and to enter into the droplets with partitioned LDH to produce lactate. To validate our hypothesis and the results just shown, we used droplets containing both urease and LDH, and droplets containing both urease and PK. Upon activation of urease and PK (with their substrates), the amount of lactate produced (Fig. 4C, yellow squares and line) is the same as the negative control in the first minutes, confirming the separate localization of the two enzymes in separate droplets. Interestingly, after 5-10 minutes, the production of lactate accelerates reaching the rate of the positive control which indicates co-localization of the enzymes with an increased efficiency of lactate production due to droplet migration, merging and forced mixing. This result confirms the experiments obtained using the confocal microscope and reported in Fig. 4A and B.

Discussion

In the last decade, a wide pool of *in vitro* protocell systems have been generated. Spanning from membrane-embedded to membraneless protocells, they imposed themselves as key tool to study biochemical features of the cell and provide the basis for the creation of new materials. Reproducing cellular behavior *in vitro* is essential to understand how living cellular systems work and interact. However, mimicking cellular complexity *in vitro* is still challenging due to limitations of the current protocell systems.

Here, we have demonstrated that membraneless enzymatically-active droplets respond and explore their surroundings triggered by a pH gradient in a chemotactic manner. Thus, our synthetic droplets mimic cytosolic protein crowding conditions and are able to sense and migrate to the neighboring droplets by following the chemotactic gradient produced through enzyme activity. Each active droplet is enzymatically producing ammonia, generating a pH gradient that is strongly related to the droplet size (Fig. 2A), which extends outside the droplets as a pH halo. The pH change modifies the surface tension of the droplet [50], triggering a Marangoni-induced flow, which drives the migrations of the droplets towards the neighboring ones. The migration velocity is determined by the surface tension gradient along the interface of the droplet: larger surface tension gradients result in higher migration speeds. Surface tension changes according to the local pH value, as indicated in Fig. S6; experimental measurements indicate that relevant changes in surface tension are only achieved in a relatively narrow range of pH, approximately within pH= 7.5-= 8.5. Small droplets (radius <25-30 μm) have a low internal pH (pH $\leq$7.5) and are able to produce only small changes in pH and negligible changes in surface tension. Thus, small droplets, even when close to each other, do not display any migration, as shown in Fig. 3A: the surface tension at the interface is almost constant, thus not producing any relevant Marangoni-induced flow. Large droplets (radius >35-40 μm) are instead characterized by higher values of internal pH, well within the range where surface tension changes occur. We can observe a two-fold effect of the internal pH: (i) it sets the surface tension

(and its changes) at the interface of the droplet and (ii) it determines the width of the pH halo extending from the edges of the droplets. Both these factors are important in determining the migration of the droplets: for a droplet to move, it must interact with the halo produced by another droplet further away and the pH changes due to the droplet-halo interaction must generate a surface tension gradient. The general trend shows that: (i) large droplets (radius >35-40 μm) migrate and merge with the neighbouring droplets within 1-2 mins after the addition of the enzyme substrate (115 mM urea), and (ii) no migration is displayed when either there is no pH change along the droplet's interface or the internal pH of the droplet is low (pH < 7.5), Fig. 3A.

The experimental data on the migration of the droplets were confirmed by numerical simulations. The droplets move against the surface tension gradient present along their interface, in agreement with experimental observations. The Marangoni-induced flow, directed from low-surface tension (high pH) regions towards high-surface tension (low pH) regions pushes the droplet towards the low-surface tension region. We confirm that internal pH is the key factor in ultimately determining the motility of the droplets by setting (i) the surface tension at the interface and (ii) the extension of the pH halo off the interface. We observe indeed that when the droplets are small (as in Fig. S5) the internal pH is too low and no motion is observed. Larger droplets, as those considered in Fig. 3B-D, show instead self-propelled motion, as they are larger and their internal pH is higher as shown in Fig. 2A. It is interesting to note that we observe also small droplets moving as in Fig. 3C. This observation however does not contradict our findings: the smaller droplet is moving as it is well within the halo produced by the larger droplet, causing a strong imbalance in the pH (and surface tension) values along the interface of the smaller droplet, and thus Marangoni-induced motion. The imbalance in the pH distribution is visible in the simulation snapshots as a pH hotspot on the left side of the smaller droplet (i.e. the side facing the larger droplet). There, surface tension is lower and the Marangoni-induced flow shifts the smaller droplet towards the larger one. We are thus able to provide a physics-aware explanation of the chemotactical migration and interaction of droplets and to reproduce these findings with numerical simulations.

The mechanisms we described here could represent an ancient chemotactical sensing mean, which arose before the development of complex cellular machinery of chemotaxis, which could play a key role in an origin of life scenario. This basic chemotactical sensing could have driven the emergence of metabolic pathways. To support this hypothesis, we showed how the migration of droplets can facilitate the formation of a short metabolic pathway. In this experiment the enzyme triggered migration leads to (i) localization of the metabolic pathway in a single droplet, (ii) mixing due to the inner Marangoni-induced flow and (iii) increased yield of the final product. Specifically, droplet migration speeds up the final product yield to the same levels of pre-localized control within the first 15 minutes of the reaction.

This study is a step forward (i) to increase the degree of complexity of artificial protocells to mimic cellular features, (ii) to reduce stability and membrane-related diffusion limitations [46], and (iii) it can integrate the recent advances in this field

[18, 19, 30, 35, 40, 41]. It is also an essential step for assessing biologically-relevant questions related to long-range interactions and chemotactical sensing. Furthermore, these results show the relevance of fluids mechanics in ubiquitous biological processes such as chemotactical sensing and migration, opening up interesting new perspectives as synthetic biological tool, as a drug delivery system and bio-inspired smart materials.

Figures

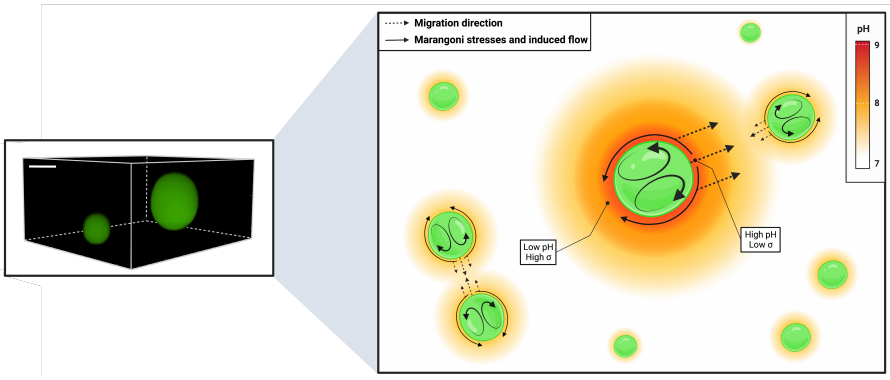

Fig. 1 Active membraneless droplets show migration governed by a chemical gradient. Z-stack visualization of the droplets containing Alexa Fluor 488 labeled-BSA (green) using PEGDA 10 kDa as a glass slide coating (left) and schematic representation of pH driven droplets migration (right). Active urease-containing droplets (1-1.5 μM) after adding 115 mM urea are able to generate a pH gradient which affects the droplet surface tension accordingly. This physical phenomenon triggers the Marangoni stresses and inner re-circulation flow in the droplets, which leads the migration towards higher pH (lower surface tension σ), i.e. towards the neighbouring droplets. In detail, droplets with a large radius show a higher pH gradient (which extends outside the droplet) and merge faster compared to droplets with smaller radius. Scale bar 20 μm.

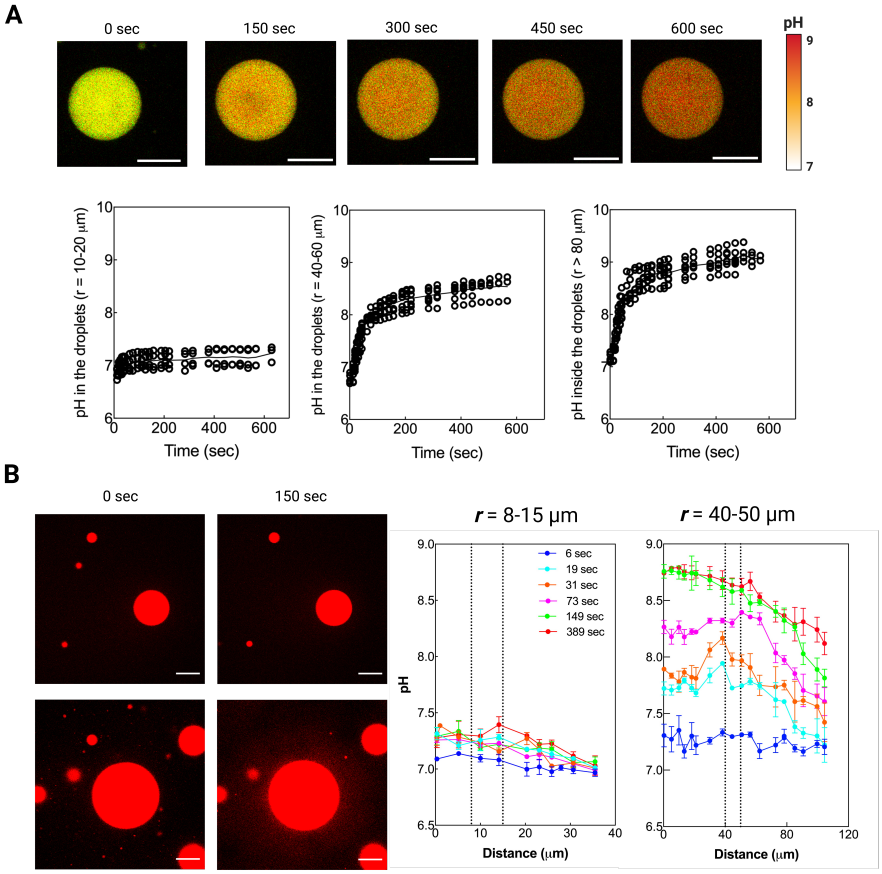

Fig. 2 The pH gradient inside and outside the droplets is related to droplets size. A. Top to bottom: BSA labeled with the pH-sensitive probe SNARF were used for the visualization of the pH changes inside a droplet containing 1-1.5 μM urease using 115 mM urea at different times. Evaluation of the pH change over time for droplets with different radius containing 1-1.5 μM urease using 115 mM urea. BSA-labeled with SNARF-1 pH probe were used for the ratiometric quantification of the pH change inside the droplets (see Materials and Methods section). Data are represented with all the dataset collected during the experiments. **B.** confocal images of active droplets with different size containing 1-1.5 μM urease upon addition of 115 mM urea in presence of BSA labeled with SNARF and free SNARF 50 μM (only the red channel is shown). Evaluation of the pH gradient around the droplets (halo, only red channel is shown) at different times using droplets with different size (between 8-15 μm and around 40-50 μm). Data are represented with at least three different droplets in the size range reported. Scale bar 50 μm.

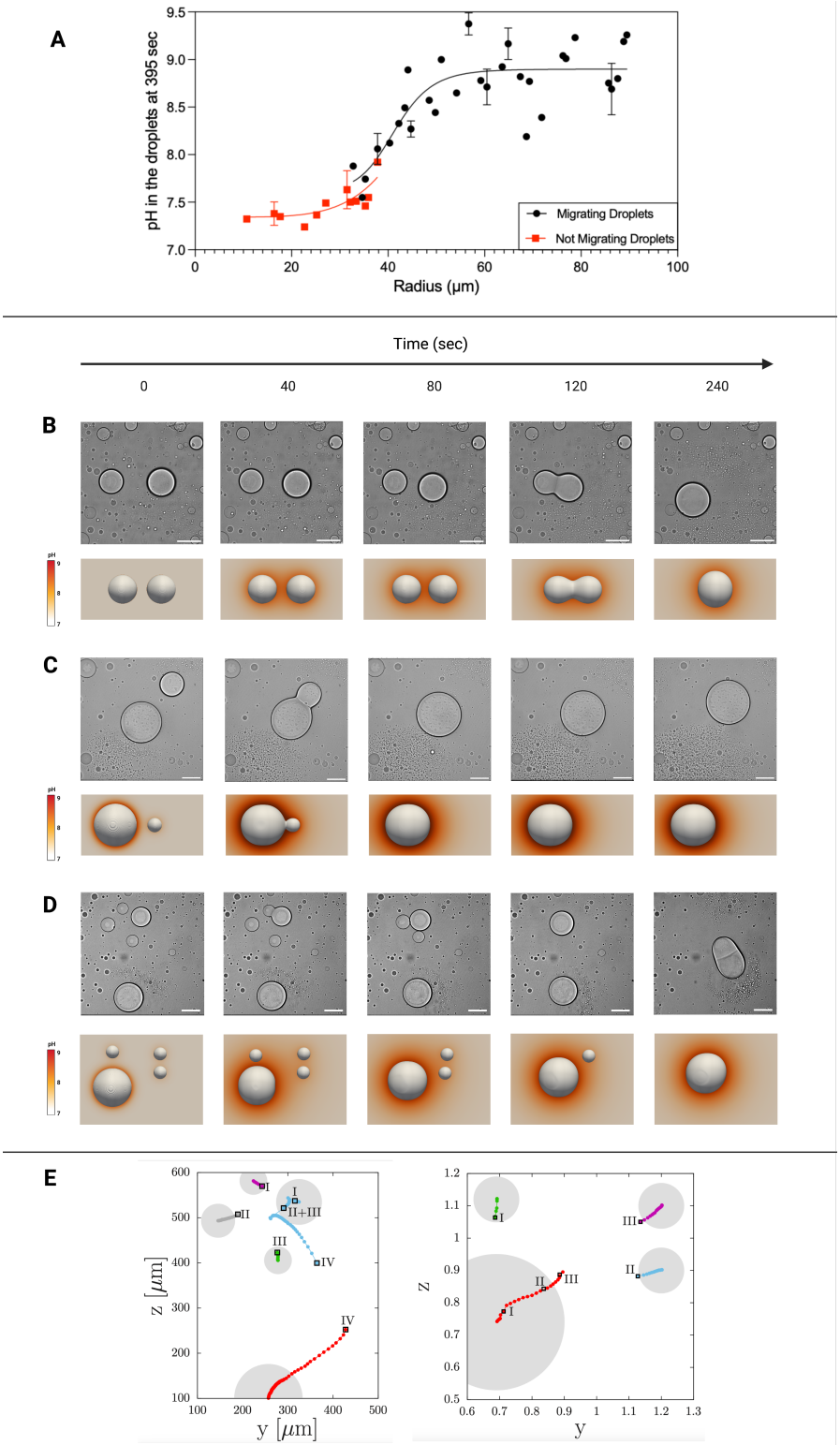

Fig. 3 The migration mediated by the pH change of the active droplets is influenced by the droplet's size. A. The graph shows the relation between droplets size and their internal pH. Red dots represent the droplets which do not show migration, while black dots highlight the droplets which show migration. Lines represent the sigmoidal fitting of the two datasets. More than 50 active droplets with different size were analyzed which contain 1-1.5 μM urease in presence of the substrate urea (115 mM). **B-D.** Top: visualization at different times of active droplets of similar size containing 1-1.5 μM urease in presence of 115 mM urea which show migration and merging in solution. Scale bar: 100 μm. Bottom: numerical simulations of the droplets supporting the experimental evidence (Supporting Movie 10, 11 and 12); the simulation snapshots shown are taken at different times. **E.** Trajectory analysis performed by tracking the center of the droplets of the experiment (left) and numerical simulation (right) reported in panel D. Different colors represent the center of different droplets over time; markers are drawn every $\Delta T = 6$ sec (experiment, left) and $\Delta T = 0.04$ (simulation, right). The droplets' trajectory have been analysed using MATLAB software. Each merging event is numbered (I-IV, experiment and I-III simulation) and highlighted with black empty squares.

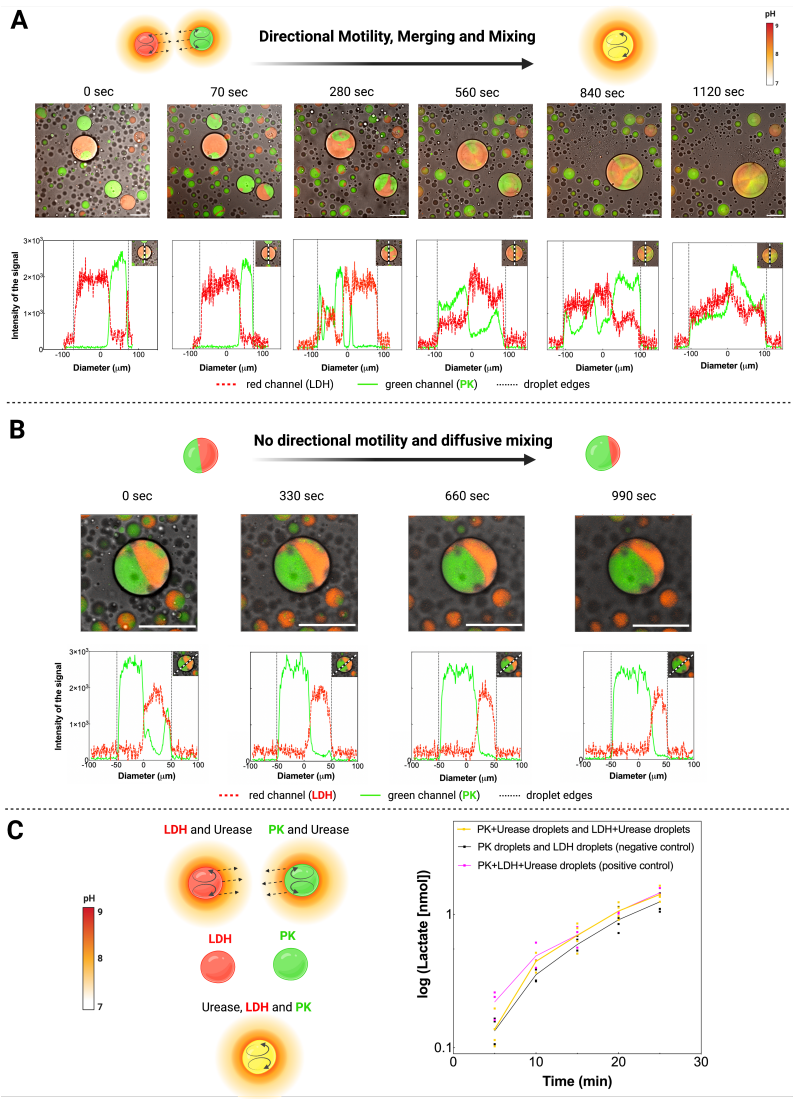

Fig. 4 The formation of a short protometabolic pathway is driven by the migration of the active droplets. A. Top to bottom: snapshots at different times of active droplets containing 1 μM urease (not labeled) and 3.3 μM Alexa Fluor 488 labeled-LDH in presence of active droplets containing 1 μM urease and 3.3 μM Alexa Fluor 594 labeled-PK which display migration, merging and forced mixing mediated by the internal flow (when activated by adding 115 mM urea). At the bottom are reported the intensity of the green (Alexa Fluor 488 labeled-LDH) and red channel (Alexa Fluor 594 labeled-PK) which are changing during time due to the mixing of the droplet content. Scale bar 100 μm. **B.** Snapshots of active droplets at different times containing 3.3 μM Alexa Fluor 488 labeled-LDH and 3.3 μM Alexa Fluor 594 labeled-PK without partitioned urease. Intensity of the green and red channel at different times are superimposed which indicates a slow and diffusive mixing. Scale bar 100 μm. **C.** Evaluation of lactate produced by LDH using three different set ups. Purple squares and line represent the positive control, based on active droplets (in presence of urea 115 mM, phosphoenolpyruvate 1 mM, NADH 2 mM and ADP 2 mM) containing 1 μM urease, 3.3 μM PK and 3.3 μM LDH; Black squares and line represent the negative control of the experiment, based on active droplets (in presence of urea 115 mM phosphoenolpyruvate 1 mM, NADH 2 mM and ADP 2 mM) containing either 3.3 μM LDH or 3.3 μM PK, in separated droplets. In the last set up, yellow squares and line represent active droplets (in presence of urea 115 mM, phosphoenolpyruvate 1 mM, NADH 2 mM and ADP 2 mM) containing 1 μM urease with 3.3 μM LDH and droplets containing 1 μM urease with 3.3 μM PK.

Material and Methods

Materials

Polyethylene glycol (PEG) 4000 Da (A16151) was purchased from Alpha-Aesar. Bovine serum albumin (BSA) (A7638), Potassium phospate dibasic trihydrate (60349), 3-(Trimethoxysilyl)propylmethacrylate (440159), 2-Hydroxy-4'-(2-hydroxyyethoxy)-2-methylpropiophenone (410896), Poly(ethylene glycol) diacrylate (PEGDA) 700 Da (455008), PEGDA 4 kDa (907227), PEGDA 6 kDa (701963), PEGDA 10 kDa (729094), L-lactate dehydrogenase (LDH) from muscle rabbit (L1254), Pyruvate Kinase (PK) from muscle rabbit (P9136), Jack bean urease (U4002), β-Nicotinamide adenine dinucleotide reduced disodium salt hydrate (NADH) (N8129), Phosphoenolpyruvate (860077), Lactate assay Kit (MAK064), Pyrydoxal 5'-phosphate (PLP) (P9255), glucose (G8270) and β-chloro-L-alanine (C9033) were purchased from Sigma-Aldrich. Potassium phosphate monobasic (42420) and trichloroacetic acid (TCA) (34603) was purchased from Nacalai Tesque. Alexa Fluor 594 and 488 Microscale Protein Labeling Kit (A30008 and A30006), Succinimidyl Ester SNARF-1 (S2280) were purchased from Thermo Fischer Scientific.

Glass coating slides preparation

Glass slides (VWR) were cleaned using water and ethanol and let to dry out for a few minutes. The clean glass slides were pre-treated with a 0.3% v/v 3-(trimethoxysilyl) propylmethacrylate dispersed in a 5% v/v ethanol-water mixture and then quenched adding pure ethanol. At this point a solution of the UV activated initiator 2-Hydroxy-4'-(2-hydroxyyethoxy)-2- methylpropiophenone at 1% w/w was prepared in water, and then added it to PEGDA 700 or 4000, 6000 or 10000 Da in a 80/20 initiator solution to PEGDA v/v ratio. 30 μL of the PEGDA-initiator mixture were pipetted on a pre-treated glass slide, and another clean, untreated glass slide (coated with an anti-rain film) was deposited on top. A thin layer of the PEGDA initiator mixture was allowed to spread via capillary action between the two glass slides to create a uniform coating. The glass slides were put under a UV lamp for 10 minutes and then stored underwater.

Protein labeling

Bovine serum albumine, urease, cystalysin, pyruvate kinase and Lactate dehydrogenase were tagged as reported previously [50]. The reaction between SNARF-1 and BSA was carried out in water for 60 minutes at room temperature. All the tagged proteins were further purified using membrane dialysis to reduce the free probe in solution. The protein concentration of BSA, urease and Lactate dehydrogenase was measured as reported previously [50]. To determine the concentration pyruvate kinase we used $\varepsilon_{280nm} = 30410$ M^{-1} cm^{-1} (https://web.expasy.org/protparam/) while the method for the quantification of cystalysin is reported in the Supplementary Information, Sec. Expression and purification of cystalysin. The degree of labeling of the proteins with the fluorescent probes was evaluated by following the manufacturer's protocol (Microscale Protein Labeling Kit, ThermoFisher Scientific).

Confocal imaging

All fluorescence and brightfield images were acquired and analyzed using a Spinning Disk Confocal (Nikon, Andor CSU) an LSM 880 Airyscan (Carl Zeiss Microscopy) microscopes with 63× oil immersion lens, 40×/1.30 PlanApo oil lens and 20× lens. Confocal images were acquired for more than 3-5 independent experiments with similar results. The images collected were analyzed using ImageJ.

pH Imaging and halo measurements

We quantified the pH variations inside the droplets using fluorescence ratiometric imaging as reported here [50]. After labelling BSA with SNARF-1 (with minor modifications from the previous protocol, by adding 100 μM SNARF-1 as final concentration to the BSA solution), SNARF-1 labeled BSA was used to make droplets following the procedure reported in the section "Droplets preparation" in SI, with a final concentration of 1 μM for urease, 33 μM Cystalysin and 33 μM Glucose oxidase inside the droplets. Note that the enzymes were not labeled with any fluorescent probe but the partitioning of the enzymes inside the droplets have been evaluated and reported here Fig. S2. To measure the halo around the active droplets free SNARF-1 probe was added to the supernatant phase at a final concentration of 50 μM and added to the droplets along with the substrate. Briefly, the droplet solution was centrifuged for 30 seconds at 16900 g at room temperature and roughly more than half of the total supernatant was removed from the microcentrifuge tube. The droplets phase was gently resuspended and 2 μL was diluted in 18 μL of free supernatant and added to the sample chamber. Then 180 μL of supernatant containing the substrate and free SNARF-1 were added to the sample chamber and the measurement started. A confocal microscope LSM 880 Airyscan (Carl Zeiss Microscopy) has been used to image the pH inside and outside the droplets. A 40×/1.30 PlanApo oil lens has been used for all the experiments. Fluorescence imaging was performed exciting the dye at 561 nm and monitoring the pH-dependent emission spectral shifts simultaneously in two separate channels. The emission wavelengths selected were $\lambda_g = 585$ nm and $\lambda_r = 640$ nm. Only the emission fluorescence at $\lambda_r = 640$ nm has been shown in (Fig. 2B) to show the droplet halo.

Pyruvate kinase and lactate dehydrogenase activity assay

Droplet suspensions with partitioned pyruvate kinase and l-lactate dehydrogenase were prepared as reported in the previous section, adjusting the concentrations of inorganic ions and enzyme cofactors as follows: KCl 80 mM, $MgCl_2$ 5 mM, ADP 2 mM and NADH 2 mM. The final concentration of enzymes inside the droplets were 3.3 μM LDH, 3.3 μM PK and 1 μM urease. The experiments have been performed as follows. 15 μL of droplets and supernatant phase was diluted in 735 μL of supernatant phase (1:50 dilution) containing 1 mM phosphoenolpyruvate, 2 mM ADP, 2 mM NADH and 115 mM urea. At each timepoint, 45 μL of reaction mix was quenched using 5 μL of 100% Trichloroacetic acid (TCA) (dilution 1:10 v/v) and stored in ice. Then, the quenched samples were centrifuged for 10 minutes at 16000 g at RT (25°C). The amount of lactate in the reaction mix was measured with the Lactate Assay Kit

(colorimetric assay) by reading the absorbance using Multiskan SkyHigh plate reader (Thermo Fisher Scientific). Specifically, 5 μL of quenched samples were added to 45 μL of Lactate Assay Buffer (provided in Lactate Assay Kit) into a 96 well plate. At this point, 50 μL of solution (Lactate Probe + Lactate Enzyme Mix + Lactate Assay Buffer) was added to the stopped reaction mix and incubated for 30 minutes protected from light. Absorbance was read at 570 nm. Lactate from the Lactate Assay Kit was used to determine the nmoles of lactate present in the wells through the calibration curve. The data were analyzed using GraphPad Prism 9 and at least three independent experiments were performed.

Numerical method

To simulate the dynamics of the droplets we solved the incompressible Navier-Stokes equations (conservation of momentum and incompressibility constraint) coupled to the volume of fluid transport equation and to the transport equation of the concentration field determining the local pH value. The droplets were identified using a color function, the volume of fluid variable, which distinguishes the droplets from the supernatant. The multi-dimensional tangent of hyperbola for interface capturing (MTHINC) method [53, 54] was used within the volume of fluid framework to improve the accuracy in the transport of the interface and to reduce parasitic currents at the interface. The surface tension of the interface of the droplets depends on the local pH field [50]; the change in surface tension as a function of the local pH is reported in Fig. S6. An advection-diffusion equation was used to describe the transport of the concentration field determining the local value of the pH. A size-dependent source term is active within the droplets to model the chemical reaction occurring inside the droplets and increasing the pH value.

The system of equation was discretized in space using a second-order central finite difference scheme on a Cartesian, uniform grid. Time-advancement is performed using the second-order explicit Adams-Bashforth scheme.

We used the in-house flow solver Fujin (https://groups.oist.jp/cffu/code) used and validated for a variety of problems [54–57]. Further details on the numerical method can be found in the Supplementary information.

Statistics and Reproducibility

All the experimental data presented in this work have been performed in triplicate at least. The authors were not blinded during outcome assessment or in the experimental design.

Data availability

The dataset generated during the study are available from the corresponding authors on reasonable request.

Code availability

The code used for the present research is a standard direct numerical simulation solver for the Navier–Stokes equations. Full details of the code used for the numerical simulations are provided in the Methods section, in the Supplementary information, and in the references therein.

Author Contributions

M.D., A.M. and P.L. conceived the project. M.D. and P.L designed the experiments. M.D. and A.B. performed all the experiments. M.D. A.B. and P.L. analyzed the experimental data. G.S., A.M. and M.E.R. wrote the code, performed the simulations and analyzed the numerical data. P.L., M.D., A.B. G.S. and M.E.R. wrote the manuscript. This project was supervised by P.L.

Acknowledgements

The research was supported by the Okinawa Institute of Science and Technology Graduate University (OIST) with subsidy funding to P.L. and M.E.R. from the Cabinet Office, Government of Japan. M.D. thanks the financial support from Japan Society for the Promotion of Science (JSPS) for the Kakenhi Early Career Scientist N. 22K15065. P.L. thanks the financial support from Takeda Grant. We are grateful for the help provided by imaging section at OIST; in particular we thank Paolo Barzaghi for the support with the confocal microscopes. We also thank Stefano Pascarelli for the suggestions on the halo analysis, Mohamed Abdelgawad for the help with the droplet tracking analysis, Prof. Amy Shen for the initial discussion on the coating polymers and Prof. Barbara Cellini for providing the Cystalysin expression vector. The authors would also like to thank Ms Amy Gooch for critical reading. M.E.R. and G.S. acknowledge the computational resources provided by the Scientific Computing Section of the Research Support Division at OIST and the computational resources provided by HPCI under the grant hp220100. The images of the present work were prepared using Biorender.com.

Conflict of Interest

The authors declare no competing interest.

References

[1] Xavier Trepat, Zaozao Chen, and Ken Jacobson. Cell migration. *Comprehensive Physiology*, 2(4):2369, 2012.

[2] Benoit Ladoux and René-Marc Mège. Mechanobiology of collective cell behaviours. *Nature reviews Molecular cell biology*, 18(12):743–757, 2017.

[3] Guillaume Charras and Erik Sahai. Physical influences of the extracellular environment on cell migration. *Nature reviews Molecular cell biology*, 15(12):813–824, 2014.

[4] Monica A Thomas, Andrew B Kleist, and Brian F Volkman. Decoding the chemotactic signal. *Journal of leukocyte biology*, 104(2):359–374, 2018.

[5] Ineke Keizer-Gunnink, Arjan Kortholt, and Peter JM Van Haastert. Chemoattractants and chemorepellents act by inducing opposite polarity in phospholipase c and pi3-kinase signaling. *The Journal of cell biology*, 177(4):579–585, 2007.

[6] Cornelis J Weijer. Collective cell migration in development. *Journal of cell science*, 122(18):3215–3223, 2009.

[7] Henry R Hampton and Tatyana Chtanova. Lymphatic migration of immune cells. *Frontiers in immunology*, 10:1168, 2019.

[8] Peter Friedl and Katarina Wolf. Tumour-cell invasion and migration: diversity and escape mechanisms. *Nature reviews cancer*, 3(5):362–374, 2003.

[9] Hideki Yamaguchi, Jeffrey Wyckoff, and John Condeelis. Cell migration in tumors. *Current opinion in cell biology*, 17(5):559–564, 2005.

[10] Andrew D Luster, Ronen Alon, and Ulrich H von Andrian. Immune cell migration in inflammation: present and future therapeutic targets. *Nature immunology*, 6(12):1182–1190, 2005.

[11] Monica Skoge, Haicen Yue, Michael Erickstad, Albert Bae, Herbert Levine, Alex Groisman, William F Loomis, and Wouter-Jan Rappel. Cellular memory in eukaryotic chemotaxis. *Proceedings of the National Academy of Sciences*, 111(40):14448–14453, 2014.

[12] Yu Wang, Chun-Lin Chen, and Miho Iijima. Signaling mechanisms for chemotaxis. *Development, growth & differentiation*, 53(4):495–502, 2011.

[13] Dennis Bray. Bacterial chemotaxis and the question of gain. *Proceedings of the National Academy of Sciences*, 99(1):7–9, 2002.

[14] Dianqing Wu. Signaling mechanisms for regulation of chemotaxis. *Cell research*, 15(1):52–56, 2005.

[15] Rodolfo García-Contreras, Paul Vos, Hans V Westerhoff, and Fred C Boogerd. Why in vivo may not equal in vitro–new effectors revealed by measurement of enzymatic activities under the same in vivo-like assay conditions. *The FEBS journal*, 279(22):4145–4159, 2012.

[16] Shannon L Speer, Wenwen Zheng, Xin Jiang, I-Te Chu, Alex J Guseman, Maili Liu, Gary J Pielak, and Conggang Li. The intracellular environment affects

protein–protein interactions. *Proceedings of the National Academy of Sciences*, 118(11):e2019918118, 2021.

[17] Muneyuki Matsuo, Taro Toyota, Kentaro Suzuki, and Tadashi Sugawara. Evolution of proliferative model protocells highly responsive to the environment. *Life*, 12(10):1635, 2022.

[18] Pierangelo Gobbo, Avinash J Patil, Mei Li, Robert Harniman, Wuge H Briscoe, and Stephen Mann. Programmed assembly of synthetic protocells into thermoresponsive prototissues. *Nature materials*, 17(12):1145–1153, 2018.

[19] Nishkantha Arulkumaran, Mervyn Singer, Stefan Howorka, and Jonathan R Burns. Creating complex protocells and prototissues using simple dna building blocks. *Nature Communications*, 14(1):1314, 2023.

[20] David William Green, Jolanta Anna Watson, Besim Ben-Nissan, Gregory Shaun Watson, and Artemis Stamboulis. Synthetic tissue engineering with smart, cytomimetic protocells. *Biomaterials*, 276:120941, 2021.

[21] Songyang Liu, Yanwen Zhang, Mei Li, Li Xiong, Zijian Zhang, Xiaohai Yang, Xiaoxiao He, Kemin Wang, Jianbo Liu, and Stephen Mann. Enzyme-mediated nitric oxide production in vasoactive erythrocyte membrane-enclosed coacervate protocells. *Nature Chemistry*, 12(12):1165–1173, 2020.

[22] Elie Dolgin. The shape-shifting blobs that shook up cell biology. *Nature*, 611(7934):24–27, 2022.

[23] Salman F Banani, Lena K Afeyan, Susana W Hawken, Jonathan E Henninger, Alessandra Dall'Agnese, Victoria E Clark, Jesse M Platt, Ozgur Oksuz, Nancy M Hannett, Ido Sagi, et al. Genetic variation associated with condensate dysregulation in disease. *Developmental Cell*, 57(14):1776–1788, 2022.

[24] Jingjing Xie, Hao He, Wenna Kong, Ziwen Li, Zhenting Gao, Daoqing Xie, Lin Sun, Xiaofei Fan, Xiangqing Jiang, Qiangang Zheng, et al. Targeting androgen receptor phase separation to overcome antiandrogen resistance. *Nature Chemical Biology*, 18(12):1341–1350, 2022.

[25] Xavier Arquè, Marcelo DT Torres, Tania Patiño, Andreia Boaro, Samuel Sánchez, and Cesar de la Fuente-Nunez. Autonomous treatment of bacterial infections in vivo using antimicrobial micro-and nanomotors. *ACS nano*, 16(5):7547–7558, 2022.

[26] Yei-Chen Lai, Ziwei Liu, and Irene A Chen. Encapsulation of ribozymes inside model protocells leads to faster evolutionary adaptation. *Proceedings of the National Academy of Sciences*, 118(21):e2025054118, 2021.

[27] Zachary R Cohen, Caitlin E Cornell, David C Catling, Roy A Black, and Sarah L Keller. Prebiotic protocell membranes retain encapsulated contents during flocculation, and phospholipids preserve encapsulation during dehydration. *Langmuir*, 38(3):1304–1310, 2022.

[28] Irep Gözen, Elif Senem Köksal, Inga Põldsalu, Lin Xue, Karolina Spustova, Esteban Pedrueza-Villalmanzo, Ruslan Ryskulov, Fanda Meng, and Aldo Jesorka. Protocells: Milestones and recent advances. *Small*, 18(18):2106624, 2022.

[29] Yifan Lyu, Ruizi Peng, Hui Liu, Hailan Kuai, Liuting Mo, Da Han, Juan Li, and Weihong Tan. Protocells programmed through artificial reaction networks. *Chemical Science*, 11(3):631–642, 2020.

[30] BVVS Pavan Kumar, Avinash J Patil, and Stephen Mann. Enzyme-powered motility in buoyant organoclay/dna protocells. *Nature chemistry*, 10(11):1154–1163, 2018.

[31] Salman F Banani, Hyun O Lee, Anthony A Hyman, and Michael K Rosen. Biomolecular condensates: organizers of cellular biochemistry. *Nature reviews Molecular cell biology*, 18(5):285–298, 2017.

[32] Steven Boeynaems, Simon Alberti, Nicolas L Fawzi, Tanja Mittag, Magdalini Polymenidou, Frederic Rousseau, Joost Schymkowitz, James Shorter, Benjamin Wolozin, Ludo Van Den Bosch, et al. Protein phase separation: a new phase in cell biology. *Trends in cell biology*, 28(6):420–435, 2018.

[33] Anthony A Hyman, Christoph A Weber, and Frank Jülicher. Liquid-liquid phase separation in biology. *Annual review of cell and developmental biology*, 30:39–58, 2014.

[34] Clifford P Brangwynne, Christian R Eckmann, David S Courson, Agata Rybarska, Carsten Hoege, Jöbin Gharakhani, Frank Jülicher, and Anthony A Hyman. Germline p granules are liquid droplets that localize by controlled dissolution/-condensation. *Science*, 324(5935):1729–1732, 2009.

[35] Carsten Donau, Fabian Späth, Michele Stasi, Alexander M Bergmann, and Job Boekhoven. Phase transitions in chemically fueled, multiphase complex coacervate droplets. *Angewandte Chemie*, 134(46):e202211905, 2022.

[36] Leonardo Demarchi, Andriy Goychuk, Ivan Maryshev, and Erwin Frey. Enzyme-enriched condensates show self-propulsion, positioning, and coexistence. *arXiv preprint arXiv:2301.00392*, 2023.

[37] Bo-Ying Xu, Jian Xu, and Tetsuya Yomo. A protocell with fusion and division. *Biochemical Society Transactions*, 47(6):1909–1919, 2019.

[38] Kensuke Kurihara, Yusaku Okura, Muneyuki Matsuo, Taro Toyota, Kentaro Suzuki, and Tadashi Sugawara. A recursive vesicle-based model protocell with a primitive model cell cycle. *Nature communications*, 6(1):8352, 2015.

[39] Avinash Patel, Liliana Malinovska, Shambaditya Saha, Jie Wang, Simon Alberti, Yamuna Krishnan, and Anthony A Hyman. Atp as a biological hydrotrope. *Science*, 356(6339):753–756, 2017.

[40] Alan Ianeselli, Damla Tetiker, Julian Stein, Alexandra Kühnlein, Christof B Mast, Dieter Braun, and T-Y Dora Tang. Non-equilibrium conditions inside rock pores drive fission, maintenance and selection of coacervate protocells. *Nature chemistry*, 14(1):32–39, 2022.

[41] Can Xu, Nicolas Martin, Mei Li, and Stephen Mann. Living material assembly of bacteriogenic protocells. *Nature*, 609(7929):1029–1037, 2022.

[42] Alex Joesaar, Shuo Yang, Bas Bögels, Ardjan van der Linden, Pascal Pieters, BVVS Pavan Kumar, Neil Dalchau, Andrew Phillips, Stephen Mann, and Tom FA de Greef. Dna-based communication in populations of synthetic protocells. *Nature nanotechnology*, 14(4):369–378, 2019.

[43] Jing Pan, Yancheng Du, Hengming Qiu, Luke R Upton, Feiran Li, and Jong Hyun Choi. Mimicking chemotactic cell migration with dna programmable synthetic vesicles. *Nano letters*, 19(12):9138–9144, 2019.

[44] Mirco DINDO, Alessandro BEVILACQUA, and Paola LAURINO. Enzymes and liquid-liquid phase separation: A new era for the regulation of enzymatic activity. *Seibutsu Butsuri*, 63(1):12–15, 2023.

[45] John T King and Anisha Shakya. Phase separation of dna: From past to present. *Biophysical Journal*, 120(7):1139–1149, 2021.

[46] Evan Spruijt. Open questions on liquid–liquid phase separation. *Communications Chemistry*, 6(1):23, 2023.

[47] NO Young, Jo S Goldstein, and MJ0087 Block. The motion of bubbles in a vertical temperature gradient. *Journal of Fluid Mechanics*, 6(3):350–356, 1959.

[48] Srigokul Upadhyayula, Timothy Quinata, Stephen Bishop, Sharad Gupta, Noah Ray Johnson, Baharak Bahmani, Kliment Bozhilov, Jeremy Stubbs, Pamela Jreij, Pratima Nallagatla, et al. Coatings of polyethylene glycol for suppressing adhesion between solid microspheres and flat surfaces. *Langmuir*, 28(11):5059–5069, 2012.

[49] Piyapong Buahom. Measuring the contact angle using imagej with contact angle plug-in. *ResearchGate*, 2018.

[50] Andrea Testa, Mirco Dindo, Aleksander A Rebane, Babak Nasouri, Robert W Style, Ramin Golestanian, Eric R Dufresne, and Paola Laurino. Sustained enzymatic activity and flow in crowded protein droplets. *Nature Communications*, 12(1):6293, 2021.

[51] Renato Fani. The origin and evolution of metabolic pathways: why and how did primordial cells construct metabolic routes? *Evolution: Education and Outreach*, 5(3):367–381, 2012.

[52] Renato Fani and Marco Fondi. Origin and evolution of metabolic pathways. *Physics of Life Reviews*, 6(1):23–52, 2009.

[53] Satoshi Ii, Kazuyasu Sugiyama, Shintaro Takeuchi, Shu Takagi, Yoichiro Matsumoto, and Feng Xiao. An interface capturing method with a continuous function: the thinc method with multi-dimensional reconstruction. *Journal of Computational Physics*, 231(5):2328–2358, 2012.

[54] Marco E Rosti, Francesco De Vita, and Luca Brandt. Numerical simulations of emulsions in shear flows. *Acta Mechanica*, 230(2):667–682, 2019.

[55] A Mazzino and M E Rosti. Unraveling the secrets of turbulence in a fluid puff. *Physical Review Letters*, 127:094501, 2021.

[56] Marco E. Rosti, Prasad Perlekar, and Dhrubaditya Mitra. Large is different: Nonmonotonic behavior of elastic range scaling in polymeric turbulence at large reynolds and deborah numbers. *Science Advances*, 9(11):eadd3831, 2023.

[57] M Abdelgawad, I Cannon, and M E Rosti. Scaling and intermittency in turbulent flows of elastoviscoplastic fluids. *Nature Physics*, 0:0, 2023.